Sensing and Bio-Sensing Research 51 (2026) 100937

Contents lists available at ScienceDirect

Sensing and Bio-Sensing Research

journal homepage: www.elsevier.com/locate/sbsr

Numerical simulation plasmonic biosensor based on metal-insulator-metal waveguide for label-free and non-invasive detection of prostate-specific antigen

Asghar Molaei-Yeznabad [a], Hamid Bahador [b,*], Ghazal Abdi [c], Azadeh Nilghaz [d]

[a] Faculty of Electrical Engineering, Shahid Beheshti University, Tehran, Iran
[b] Department of Electrical and Computer Engineering, University of Mohaghegh Ardabili, Ardabil, Iran
[c] Faculty of Electrical and Computer Engineering, University of Tabriz, Tabriz, Iran
[d] Drug Delivery, Disposition, and Dynamics, Monash University, Parkville, VIC 3052, Australia

ARTICLE INFO

Keywords:
High sensitivity
Label-free cancer diagnostics
Metal–insulator–metal waveguide
Plasmonic biosensor
Prostate-specific antigen

ABSTRACT

In this work, a high-performance metal–insulator–metal plasmonic biosensor is presented and numerically investigated for label-free detection of prostate-specific antigen, which is an important biomarker for early-stage prostate cancer diagnosis. The device architecture utilizes a coupled semi-rectangular resonator side-coupled with the waveguide, in order to achieve a strong waveguide–cavity interaction. This structural configuration enables enhanced confinement of surface plasmon polaritons, and thereby improves light–matter interaction. The finite element method solution in commercial software COMSOL Multiphysics was used to do numerical simulations, where the structural parameters were optimized to maximize sensitivity, spectral sharpness, and achieve a narrower transmittance spectrum. After optimization, the designed sensor was systematically examined for its performance in prostate-specific antigen detection. The proposed sensor achieves a sensitivity of 1872.3 nm/RIU, a narrow full width at half maximum of 24 nm, a figure of merit of 76.6 RIU^{-1}, a Q-factor of 60.3, and a limit of detection of 0.0108 RIU. Furthermore, the simple geometry and compatibility with scalable nanofabrication techniques emphasize its potential application in real-time, portable, and point-of-care cancer diagnostics.

1. Introduction

1.1. Motivation

Prostate Cancer (PC) remains one of the most commonly diagnosed cancers and one of the leading causes of cancer-related death among men in the world [1,2]. In 2021 alone, 236,659 new cases and 32,563 deaths were reported, with a five-year survival rate nearing 100 % when the disease is localized but dropping sharply to approximately 33 % once metastasis occurs [1,3]. Although considerable progress has been made in the detection and monitoring of prostate cancer, existing screening modalities, including Prostate-Specific Antigen (PSA) testing, Digital Rectal Examination (DRE), and tissue biopsy, remain constrained by notable limitations. [1]. PSA lacks specificity, DRE is invasive and unreliable, and biopsies, though the gold standard, are invasive with risks and sampling errors [1]. Although substantial progress has been made in diagnostics, from imaging techniques like Magnetic Resonance Imaging (MRI) and Computed Tomography (CT) scans to molecular methods such as Polymerase Chain Reaction (PCR) and Enzyme-Linked Immunosorbent Assay (ELISA), these approaches are often costly, invasive, time-consuming, and sometimes harmful due to radiation exposure [4]. Consequently, there is a growing demand for rapid, sensitive, and non-invasive diagnostic technologies [2,5]. Optical biosensors, especially plasmonic sensors, have gained prominence for their ability to detect cancer-related biomarkers with high sensitivity and specificity [2]. The development of novel biosensing platforms targeting PSA could improve early PC detection, reduce unnecessary invasive procedures, and ultimately decrease mortality rates by enabling timely therapeutic interventions [3]. Plasmonic biosensors exploit the excitation of Surface Plasmon Polaritons (SPPs), which arise from the collective oscillations of free electrons at a metal-dielectric interface under electromagnetic excitation [6–8]. The intense confinement of the plasmonic field enables

* Corresponding author.
E-mail address: hamid.bahador@uma.ac.ir (H. Bahador).

https://doi.org/10.1016/j.sbsr.2025.100937
Received 15 October 2025; Received in revised form 2 December 2025; Accepted 4 December 2025
Available online 6 December 2025

these devices to overcome the diffraction limit, thereby enhancing light–matter interactions for signal transmission, processing, and sensing [7,9,10]. Moreover, engineered plasmonic resonances deliver strong and tunable light–matter interactions that enhance optical functionality [11–14]. Beyond conventional Lorentzian resonances, many plasmonic architectures support Fano-type line shapes arising from the interference between a narrow discrete cavity mode and a broad continuum background. These asymmetric resonances exhibit very steep spectral slopes, which can significantly enhance refractive-index sensing performance and detection resolution for low-abundance cancer biomarkers such as PSA [15].

1.2. Literature review

Among the various waveguide geometries explored, Metal-Insulator-Metal (MIM) waveguides have gained considerable attention for their simple fabrication, low propagation loss, strong confinement, and long transmission distance [16]. These structures feature a dielectric core confined between metallic layers, generating intense localized electromagnetic fields within the nanoscale gap, which markedly enhance sensitivity to refractive index variations arising from analyte binding [17]. Moreover, their planar geometry ensures excellent compatibility with microfluidic and integrated photonic platforms, thereby enabling the development of compact lab-on-chip diagnostic devices [18]. MIM-based coupled resonators also enable the emergence of sharp asymmetric Fano Resonances (FR), which result from interference between continuous and discrete states and offer a high figure of merit (FOM) and narrow Full Width at Half Maximum (FWHM), thereby enhancing biosensing resolution [7,19]. Various geometries, such as nanoparticle dimers, nanowire lattices, split semicircular ring resonators, grooves, nanorods, and coupled cavities have been employed to generate single and multiple FR modes, broadening the functionality of MIM plasmonic structures for multispectral and ultrasensitive detection [20–25]. For more explores in MIM-based plasmonic sensors other resonator architectures and tuning mechanisms can be mentioned as asymmetric cross-shaped and ring-stub resonators, hybrid arrays of square-ring, nanorod, and nanodisk resonators, disk–arc waveguides, and double-ring Dirac-semimetal metastructures, rectangular cavity with silver nano-defects [26–31]. These unique features have already been leveraged in the development of advanced diagnostic platforms. For example, the Plasmonic Array Nanohole Technology on MIM (PANTOMIM) architecture has been proposed to achieve high spectral purity by suppressing substrate-induced background signals, while ensuring efficient detection within the 800–850 nm wavelength range using low-cost silicon-based sensors. In a proof-of-concept demonstration, this design enabled rapid detection of uropathogenic *E. coli* directly from urine within 15 min, validated on a cohort of 100 patients, highlighting the translational potential of MIM-based plasmonic biosensors for real-world biomedical applications [9]. Overall, the dimensions, geometry, and alignment of the cavity in MIM waveguide-based plasmonic sensors critically affect light–matter interactions, thereby impacting the sensor's performance. This has led to the recent development of several innovative plasmonic sensor configurations. A nanowall-modified plasmonic Bow Tie resonator has been proposed to enhance refractive index sensing, achieving strong SPP confinement and a sensitivity of ~2300 nm/RIU, far exceeding the standard Bow Tie design [32]. Paper-based plasmonic refractometric sensors have been fabricated by embedding Silver (Ag), Gold (Au), and Au—Ag nanoparticles onto inkjet papers via reverse nanoimprint lithography, achieving a particle transfer efficiency of ~85 %, high refractometric sensitivity to volatile biogenic amines, and strong selectivity for monitoring food freshness [33]. A metamaterial-based triple-band biosensor operating in the PHz range has been designed for early leukemia detection, showing near-perfect absorption and superior diagnostic performance [34]. A graphene–Ag–Au plasmonic sensor operating at 0.1–1 THz has been developed for wastewater monitoring, achieving a sensitivity of 227 GHz/RIU and enhanced detection accuracy through machine learning, demonstrating strong potential for the detection of trace organic pollutants [35].

Although significant advances have been made in plasmonic biosensors for PSA detection, several key challenges still limit their clinical applicability. Many existing MIM biosensors exhibit moderate sensitivity and broad resonance peaks, which reduce the detection accuracy for early-stage diagnosis. Furthermore, inadequate optimization of coupling and field confinement mechanisms often results in low Q-factors and poor extinction ratios. Most previous studies focus on single-parameter tuning rather than the comprehensive multi-parameter optimization required for better performance. Furthermore, theoretical designs often overlook fabrication feasibility and scalability, as well as compatibility with practical techniques such as nanoimprint lithography.

This study presents a novel plasmonic biosensor that directly addresses key limitations of existing MIM-based PSA detection systems through innovative structural design and comprehensive optimization. A unique side-coupled semi-rectangular resonator configuration is proposed to enhance waveguide–resonator coupling, resulting in stronger field confinement and sharper resonance peaks. Unlike previous works that focused on isolated parameters, this research systematically optimizes four critical geometric factors: waveguide width, coupling gap, cavity length, and inter-resonator separation to achieve maximum sensitivity and spectral precision. The optimized structure demonstrates outstanding performance, with a sensitivity of 1872.3 nm/RIU, a narrow FWHM of 24 nm, a FOM of 76.6 RIU^{-1}, a Q-factor of 60.3, and a LoD of 0.0108 RIU, surpassing most reported designs. Furthermore, the biosensor's configuration is compatible with scalable fabrication methods such as nanoimprint lithography and electron beam evaporation, ensuring practical manufacturability. Targeting PSA detection, the sensor achieves label-free, real-time, and clinically relevant performance, making it highly suitable for point-of-care and microfluidic diagnostic applications.

The article is divided into the following sections: in the second part, the necessary methodologies for this type of sensor are presented. This stage also includes the manufacturing process and its explanations. In the third part, the simulation results are presented, along with a comprehensive explanation of each. Finally, the fourth part is dedicated to the general conclusion, and future trends are presented in this section.

2. Device design and numerical model

In this study, a new plasmonic sensor configuration is introduced, and its transmission spectrum and H-field distribution are evaluated in comparison with conventional plasmonic sensor designs. In the standard configuration, a semi-rectangular resonator is laterally coupled to a MIM waveguide, as shown in Fig. 1(a) and Fig. 1(b). The width of the MIM waveguide is shown by W, and its total length is represented by L. The coupling gap between the waveguide and the cavity is indicated by g. Inside the resonator, the cavity arm length is defined as l, while the arm width is represented by a. The inner section of the cavity is further described by the parameters b and c, which correspond to the inner arm length and width, respectively. The separation between the two cavity

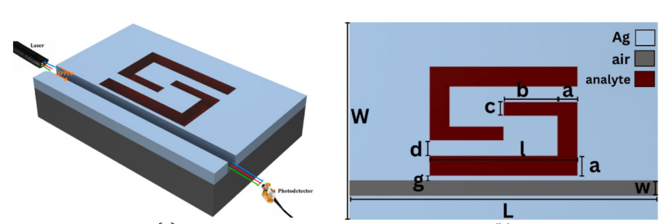

Fig. 1. MIM sensor schematic design with coupled semi-rectangular resonator; (a) 3-D view of the designed sensor; (b) 2-D view from the top of the sensor with parameters.

branches is shown as d. The dielectric medium inside the cavity is filled by the analyte, while the surrounding material is Ag, as shown in the schematic. Table 1 provides the initial settings of the device's structural parameters. Among various plasmonic materials, Ag is widely recognized as a suitable candidate owing to its pronounced surface plasmon resonance (SPR) response across the visible and near-infrared regions of the electromagnetic spectrum. This characteristic arises from the distinct electronic structure of Ag, enabling electron oscillations in the metal to strongly couple with incident light waves. It is also worth noting that initial FEM scans showed that moderate variations of these dimensions mainly cause a nearly rigid resonance shift with minor changes in damping, while excessively small or large values either violate fabrication constraints or unnecessarily increase the footprint of the part without improving the sensitivity-performance of the FOM. Therefore, in this work, the internal cavity parameters a, b and c were kept constant.

It should be noted that the geometric values in Table 1 are not arbitrarily chosen. They are extracted from recently reported MIM resonator-waveguide sensors with similar operating wavelengths and then adjusted to meet realistic nanofabrication constraints (minimum feature size, metal thickness, and surface area). This basic geometry provides a physically and technologically acceptable starting point from which the key parameters w, g, l, and d are systematically optimized.

2.1. Numerical simulation details

In this section, an attempt has been made to provide more details of the simulation process to increase the repeatability of the study so that further progress can be made in this area in future work. The simulation details with full explanations of each section are mentioned below. The proposed plasmonic biosensor has been numerically and 2D simulated using COMSOL Multiphysics version 6.3 software. In this paper, all simulations are performed using a 2D finite element method (FEM) model to solve Maxwell's equations governing the propagation of electromagnetic waves. The proposed MIM waveguide-amplifier system is translationally invariant in the out-of-plane direction, so the TM SPP ground state is fully described in the cross section. For such structures, the 2D and 3D models essentially give the same resonant and sensing behavior, while the 2D models greatly reduce the computational cost and enable extensive parametric optimization [36]. The interface of Electromagnetic Waves, Beam Envelopes (EWBE), was selected, and the study was carried out in the wavelength domain. In the physics settings section, the three-component vector option was selected for components, and the bidirectional option was selected for the wave vector section. The rest of the items were taken as default. To excite the structure, a periodic source with an input power of 1 W/m2 was applied to excite the guided modes, while the output transmission spectra were recorded to evaluate the sensing performance. Two input and output ports were also defined as periodic. The input port (Pin) was defined to excite SPPs at the metal-dielectric interface, and the optical response of the device was measured by monitoring the transmission spectrum at the output port (Pout). Both TM and TE polarizations were used to evaluate the sensor, and TM polarization was finally selected as the main polarization. Since one of the main goals of this paper is to observe the points that occur in the operational state and are different from the ideal conditions, the SBC boundary condition was used. The Perfectly Matched Layer (PML) is an artificial absorbing region that gradually absorbs the wave and creates almost zero reflection, which is less likely to occur in the operational state. However, the Scattering Boundary Condition (SBC) is a boundary condition that is applied only at the boundary and reduces the reflection, but there may be a very small amount of reflection that may also occur in the operational state. Therefore, testing the sensor in these conditions is one step closer to the operational state, and we can rely more on its outputs. Next, the structure meshing was performed. For this, the physics-controlled mesh option was selected in the sequence type section, and the element size used was also considered extremely fine to increase the accuracy of the calculations. It should be noted that the mesh type used was also selected as a triangular mesh. In the geometry section, the desired structure was drawn using the sketch option. The sensor geometry consists of an Ag plasmonic layer deposited on a SiO2 substrate, and air acts as the insulating/waveguide region. A semi-rectangular coupled analyte region, representing the PSA, was introduced into the sensing channel. The properties of the materials used in the simulations are summarized in Table 2. In the material section, using the software's own library, the refractive index of SiO_2 was taken from Goosh (1999) in the wavelength range of 0.198–2.05 μm, while the mixed refractive index of Ag was taken from the experimental data of Babar and Weaver (2015) covering 0.207–12.4 μm. The refractive index of air was modeled according to Mathar (2007) for 1.3–2.5 μm. The PSA analyte layer was represented as a dispersed medium with variable refractive index values to mimic biomolecular binding. In the study section, the wavelength domain was selected, and the frequency range was selected from 1.36 μm to 1.6 μm with a step size of 0.001207 μm. In the results section, to extract one-dimensional graphs and two-dimensional profiles after running the simulation, several plots are provided by default by physics, but to extract the norm of electric and magnetic field profiles, you must act as follows: First, a 2D Plot Group must be added in the results section. Then, this Plot must be selected, and a Surface Plot added. Then, depending on which profile is desired, the Experiment section is selected. Then, in the search box, the phrase Electric field norm or the phrase ewbe.normE is selected for the electric field profile, and Magnetic field norm or the phrase ewbe.normH is selected for the magnetic field profile. Finally, by selecting the plot option, the relevant graph is displayed. To extract graphs related to transmittance, the same process is performed similarly, with the difference that instead of the 2D Plot Group, a 1D Plot Group is used, and then a global plot is selected. Then, in the Experiment section, the phrase transmittance is searched. Depending on which port the output is, the corresponding expression is selected, which in this study is Transmittance, port 2 or ewbe. Tport_2. The rest of the available settings were selected as defaults for the physics used and the software.

As is clear, this paper aims to investigate and design a biosensor for the diagnosis of PSA disease. The proposed biosensor detects the disease based on the changes in the refractive index of different samples of PSA analyte. Experimentally, the refractive indices corresponding to each of the different concentrations of this disease were measured and are shown in Table 3 [37].

However, it should be noted that although the present model is formulated based on volumetric RI changes, in real clinical matrices

Table 1
The initial values of the proposed sensor variables.

Variable	Symbol	Value (nm)
Width_1 of the rectangular resonator arm	a	65
Length_1 of the rectangular resonator arm	b	175
Width_2 of the rectangular resonator arm	c	45
Distance between the two resonator sections	d	50
Distance between resonator and waveguide	g	15
Waveguide length	L	1000
Length_2 of the rectangular resonator arm	l	480
Substrate width	W	650
Waveguide width	w	50

Table 2
Material properties used in simulation.

Name	Material	Refractive Index
Substrate	SiO_2	Goosh 1999 (0.198 um- 2.05 um)
Metal	Ag	Ag (Silver) (Babar and Weaver 2015: n,k 0.207–12.4 um)
Insulator	Air	Air (Mathar 2007: n 1.3–2.5 um)
Analyte	PSA	Table 3

Table 3
PSA refractive index for different concentrations.

Concentration (pMPSA)	Refractive index ($n_0 + \Delta n$)
Normal	1.33
50	1.3388
100	1.3477
200	1.3654
300	1.3831
400	1.4008
500	1.4185

such as serum or urine, nonspecific adsorption and bulk RI fluctuations can induce additional resonance shifts. In a practical PSA assay, the metal surface in the cavity region would be functionalized with a thiolated self-assembled monolayer, followed by EDC/NHS activation and covalent immobilization of anti-PSA antibodies, and subsequent backfilling or blocking (e.g., PEGylated thiols or BSA) to suppress nonspecific adsorption. Specifically bound PSA molecules then form a thin biomolecular layer with an increased local refractive index in the hotspot region, so that the large bulk RI sensitivity reported here directly translates into strong responsivity to PSA binding on the functionalized surface [38–43].

Beyond its remarkable optical features, Ag offers additional advantages, such as biocompatibility and chemical stability, which further enhance its potential for biosensing applications. To describe the dielectric function of Ag, the Lorentz–Drude model is employed [44–46] as expressed in Eq. (1):

$$\varepsilon(\omega) = \varepsilon_\infty - \frac{\omega_p^2}{\omega^2 + i\gamma\omega} + \sum_j \frac{f_j\,\omega_{p,j}^2}{\omega_{0,j}^2 - \omega^2 - i\gamma_j\omega} \tag{1}$$

where $\varepsilon_\infty = 9.0685$, $\omega_p = 135.44 \times 10^{14} rads^{-1}$, and $\gamma = 1.15 \times 10^{14} rads^{-1}$. The dispersion relation, a mathematical expression describing the propagation characteristics of SPPs, explicitly depends on the dielectric responses of both the metal and the adjacent medium to the electric field:

$$k_{SPP} = k_0\sqrt{\frac{\varepsilon_m\varepsilon_d}{\varepsilon_m + \varepsilon_d}} \tag{2}$$

And the amplitude is defined as:

$$E_d(z)\alpha e^{k_m z}, k_m = k_0\sqrt{\frac{k_{SPP}^2}{k_0^2} - \varepsilon_m} \tag{3}$$

$$E_d(z)\alpha e^{-k_d z}, k_d = k_0\sqrt{\frac{k_{SPP}^2}{k_0^2} - \varepsilon_d} \tag{4}$$

The propagation length is:

$$L_{SPP} = \frac{1}{2\mathrm{Im}(k_{SPP})} \tag{5}$$

And finally, the resonance angle that excites SPPs is:

$$n_p \sin(\theta_{res}) = \sqrt{\frac{\varepsilon_m\varepsilon_d}{\varepsilon_m + \varepsilon_d}} \tag{6}$$

To clarify the coupling mechanism between the MIM waveguide and the lateral resonator, the key decay-rate relations governing linewidth, resonance depth, and critical coupling behavior are summarized below [47]:

$$\gamma_{tot} = \gamma_i + \gamma_e \tag{7}$$

Here γ_i is the intrinsic (internal) loss rate of the resonator (material absorption, radiation) and γ_e is the external (coupling) loss rate into the waveguide. γ_{tot} sets the resonance linewidth $\Delta\omega = \gamma_{tot}$ (and thus FWHM in wavelength) [48].

$$T(\omega_0) = \left|\frac{\gamma_i - \gamma_e}{\gamma_i + \gamma_e}\right|^2 \tag{8}$$

This expression (from temporal coupled-mode theory) shows that when external and internal decay rates match (critical coupling) the through-port transmission at resonance vanishes. If $\gamma_e \gg \gamma_i$(over coupled) the dip is broad but not deep; if $\gamma_e \ll \gamma_i$ (under coupled) the dip is shallow [47].

$$\Delta\omega \cong -\frac{\omega_0}{2}\frac{\left(\int \Delta\varepsilon(r)|E(r)|^2 dV\right)_{analyte}}{\left(\int |E(r)|^2 dV\right)_{all}} \tag{9}$$

The numerator quantifies how strongly the resonator field samples the analyte; Γ (modal overlap) is defined by the fraction of stored energy in the analyte. A larger gap can reduce γ_e but increase Γ, producing a trade-off between dip depth (via γ_e/γ_i) and sensitivity (via Γ). The sensing characteristics were analyzed by varying the refractive index of the analyte region and observing the corresponding resonance wavelength shift. The sensor sensitivity (S) was defined as [49]:

$$S = \frac{\Delta\lambda_{res}}{\Delta n_d}(nm/RIU) \tag{10}$$

where $\Delta\lambda_{res}$ is the resonance wavelength shift and Δn_d is the change in analyte refractive index. High sensitivity implies that minor changes in the refractive index can induce considerable shifts in the resonance wavelength, enhancing the sensor's effectiveness for biosensing applications. The proposed optimized design amplifies this wavelength shift, thereby significantly improving the sensor's detection performance. The FWHM denotes the spectral bandwidth of the resonance peak measured at 50 % of its maximum intensity and is expressed as:

$$FWHM = \lambda_{high} - \lambda_{low} \tag{11}$$

Where λ_{high} and λ_{low} correspond to the wavelengths at half of the peak intensity. A smaller FWHM value reflects a sharper resonance profile, which enhances both selectivity and measurement accuracy. The FOM is a key parameter that integrates sensitivity and FWHM to evaluate the overall sensing performance:

$$FOM = \frac{S}{FWHM} \tag{12}$$

where S is the sensitivity (nm/RIU) and FWHM is the full width at half maximum. A higher FOM indicates that the sensor simultaneously exhibits high sensitivity and a sharp resonance peak, both of which are critical for accurate detection. The proposed design enhances the FOM by optimizing the geometric parameters of the cavity and waveguide structure.

Another important performance metric is the Quality Factor (QF), which characterizes the sharpness of the resonance and is expressed as:

$$Q = \frac{\lambda_{res}}{FWHM} \tag{13}$$

where λ_{res} denotes the resonance wavelength. A higher Q-factor implies a strongly confined and efficient plasmonic resonance with minimal energy dissipation, thereby ensuring high-resolution and label-free biosensing capability.

The last parameter for accurately determining the sensor performance is the limit of detection (LOD), which represents the lowest measurable value that the sensor can detect, defined as [5]:

$$LoD = \left(\frac{\Delta n_s}{1.5}\right) \times \left(\frac{FWHM}{\Delta\lambda_0}\right)^{1.25} \tag{14}$$

2.2. Sensor fabrication process

Nanoimprint Lithography (NIL) is a powerful and cost-effective technique for fabricating high-resolution plasmonic nanostructures. It is particularly suited for creating nanoscale features with high fidelity, making it ideal for MIM-based plasmonic biosensors. As shown in Fig. 2, the process starts with a cleaned silicon or glass substrate, prepared via sequential ultrasonic cleaning in acetone, isopropanol, and deionized water, followed by drying under nitrogen flow to ensure a particle-free surface [50,51]. Next, a thermoplastic resist, commonly PMMA (polymethylmethacrylate), is spin-coated onto the substrate. The thickness of the resist layer is carefully controlled to match the desired feature depth, generally spanning from a few tens to several hundreds of nanometers [52]. A pre-patterned mold, often made of silicon or quartz, is then pressed into the resist layer at elevated temperatures (usually 150–180 °C) and moderate pressures (typically 50–100 bars) to transfer the nanoscale features. The resist is allowed to cool while under pressure, solidifying the imprinted pattern [53]. After imprinting, residual resist removal is performed using oxygen plasma etching, which clears the thin residual layer left in the cavities and exposes the substrate in the patterned regions. This step is critical to ensure uniform deposition and high reproducibility of the plasmonic structures [54]. Following etching, the plasmonic metal layer, such as Ag or gold (Au), is deposited via electron-beam evaporation or magnetron sputtering, forming the functional metallic nanostructures [55]. Finally, the resist mold is removed using solvent lift-off (e.g., acetone) or mechanical separation, leaving the patterned metal nanostructures on the substrate. Optional surface functionalization can be performed post-fabrication to immobilize biorecognition elements such as antibodies for PSA detection. NIL allows for high-throughput, reproducible, and scalable fabrication, making it suitable for practical biosensor applications [50,51,55]. Despite its advantages, NIL presents several challenges. Challenges include pressure non-uniformity, misalignment, and residual layers, which can reduce sensor performance [51,52]. These issues can be mitigated using air-cushion pressing, precise alignment systems, optimized resist thickness, and post-imprint plasma etching [53,54]. With these strategies, NIL enables reproducible nanoscale features suitable for high-sensitivity biosensing applications.

The feasibility of the proposed structure can be justified by the available experimental results. In a critical mini-review on sensors based on MIM waveguides [56], in addition to the theoretical discussion, have presented an SEM image of a real MIM waveguide with nanometer dimensions, which shows that patterning of sub-hundred-nanometer gaps in this platform is practically possible. In another work [57], have fabricated free-standing lithium niobate nano waveguides with lengths of several tens of microns and widths of up to 50 nm with a precision of several nanometers using electron beam lithography and enhanced etching processes and tested their optical performance. Yamada [58] also mentioned in his book on the investigation of the basic properties and basic applications of silicon photonic wire waveguides an 80-nm-wide waveguide that was fabricated with high precision and imaged. In another work by Elezzabi and Sederberg [59], a nanoplasmonic silicon waveguide with a very thin gold layer with a thickness of less than 50 nm was introduced and fabricated, which was used to generate green light from the nanoplasmonic silicon waveguide. These experimental results, together with other similar reports in the literature, confirm that the fabrication of waveguides and resonators with dimensions and geometric complexity on par with the proposed semi-rectangular structure is feasible and realistic within the framework of current nanofabrication technologies.

3. Results and discussion

Before presenting the simulation results, it is important to note that all simulations and results extraction steps were performed using COMSOL Multiphysics version 6.3, and hardware with the following specifications: Core i7-14700k CPU, Nvidia RTX 4060 8 GB GPU, 64 GB DDR5 RAM, and 2 + 1 GB ROM. Also, the average time for each run was approximately 14 min and 26 s, which can vary with different meshing.

3.1. Initial results

In this study, a series of optimizations was first performed to achieve the optimal configuration. The device structure consists of a coupled semi-rectangular resonator that is side-coupled to a MIM waveguide, as illustrated in Fig. 1. The goal of this optimization was to identify the geometric parameters, such as waveguide width, cavity dimensions, and coupling gaps, that maximize the sensor's extinction coefficient, resonance sharpness, and sensitivity while maintaining spectral purity. By systematically varying these parameters and analyzing the resulting transmission spectra, we were able to determine the structure that provides the highest performance for PSA biosensing applications.

Fig. 3 presents the transmittance spectrum of the proposed sensor with its initial geometrical parameters, exhibiting distinct plasmonic resonance modes within the near-infrared range (1300–1900 nm). The sharp resonance dip corresponds to the excitation of the fundamental

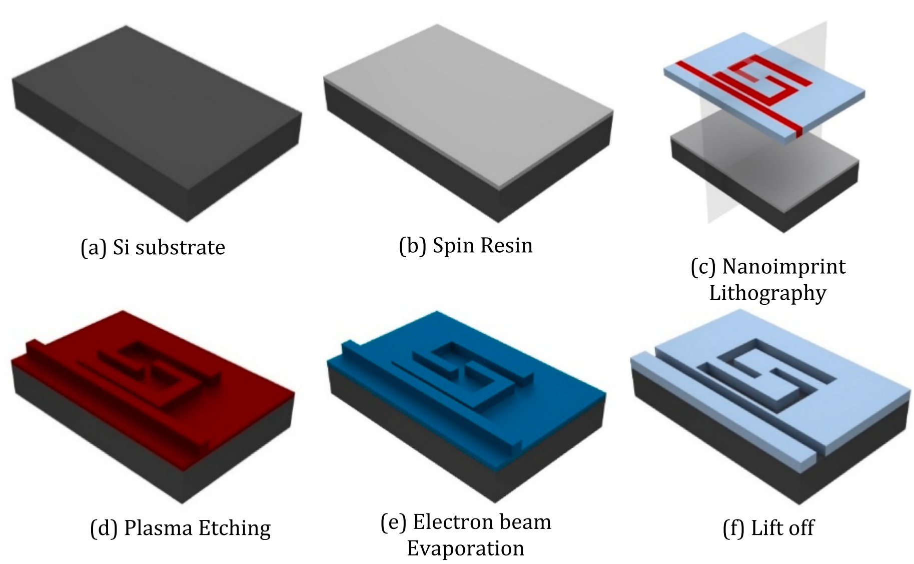

Fig. 2. Practical fabrication process of the proposed biosensor.

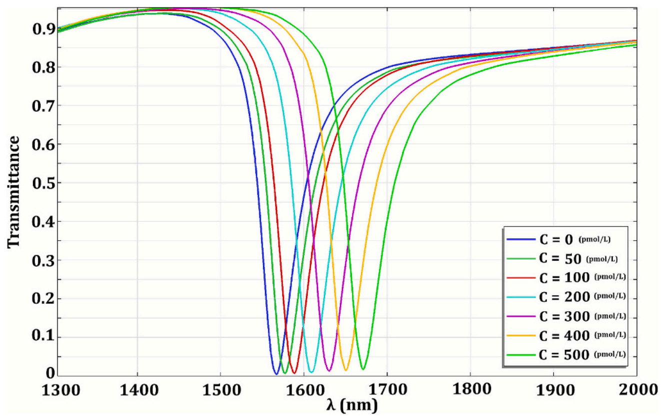

Fig. 3. Transmission spectra of the proposed sensor with initial geometrical parameters under different analyte concentrations.

SPP mode. In the reference case (n_0, corresponding to zero analyte concentration), the primary resonance dip is observed at approximately 1567.3 nm, indicating strong light confinement and absorption arising from SPP coupling at the metal–dielectric interfaces. The asymmetric line shape of the main dip evidences a Fano-type resonance from interference between the localized cavity mode and broadband MIM waveguide continuum, yielding a steeper spectral slope and enhanced sensitivity. It can be seen that, as the analyte concentration increases from $C = 50$ to $C = 500$, this resonance exhibits a pronounced red shift, moving from 1577.9 nm to 1669.3 nm. This shift confirms the high sensitivity of the device to refractive index variations induced by biomolecular adsorption. To achieve a high-performance sensor, four variables in the proposed sensor design, such as w, g, l, and d, should be tuned to achieve a narrow transmission dip and high sensitivity.

3.2. Mode analysis of the semi-rectangular cavity

In this section, we attempt to show the field distributions of the cavity mode structure, which, in a way, explain the main dip and the weaker resonances in Fig. 3. Fig. 4 shows the mode characteristics of the waveguide at resonant wavelengths. Fig. 4(a) shows the fundamental cavity mode, where the normalized field intensity exhibits a unity maximum near the cavity center with no internal nodes in either transverse direction. The nearly concentric contours and arrows of the circulating power flow indicate a lowest-order quasi-Fabry-Perot mode ($m = 1$) with uniform phase and strong confinement inside the analyte region. Fig. 4(b) shows the first higher-order longitudinal mode: two intensity lobes appear side by side inside the cavity, separated by a central node region. This pattern corresponds to a standing wave with an internal node ($m = 2$) where neighboring lobes are out of phase and the power flow is split into two opposite circulating loops. Fig. 4(c) shows a second higher-order mode with four distinct lobes and two orthogonal nodal lines, effectively combining first-order variations along both transverse directions (m,n) = (2,2) in a two-dimensional notation. The associated power flow lines confirm that energy circulates in four smaller subcavities, leading to increased propagation losses and weaker coupling to the bus waveguide. Together, these plots show that the dominant sensing resonance arises from the fundamental cavity mode, which is strongly coupled to the TM_0 plasmon-gap mode of the MIM bus, while higher-order modes only produce additional, weaker spectral features when the geometric parameters are deliberately out of tune. Specifically, the dominant dip in Fig. 3 is due to the excitation of the fundamental mode in panel (a), while the higher-order modes in panels (b) and (c) are the origin of the sub-resonances and spectral changes when changing the geometric dimensions.

3.3. Sensor optimization

In the first optimization step, the waveguide width (w) is varied while keeping all other parameters fixed at their initial values, as listed in Table 1. With the refractive index set to 1.33, w is adjusted from 10 nm to 80 nm in increments of 10 nm to determine the optimal effective width that ensures maximum confinement of the resonance wavelength (λ_{res}). The corresponding transmittance spectra for this variation are presented in Fig. 4. It can be observed that for narrow widths ($w < 40$ nm), both the resonance wavelength and the FWHM exhibit significant variations, and the *E*-field confinement in the cavity is not too strong, resulting in the broader transmission dip. However, for $w \geq 40$ nm, the resonance wavelength remains nearly constant, while the waveguide width mainly affects the FWHM. Generally, varying the waveguide width w mainly tunes the propagation constant and confinement of the fundamental TM gap-plasmon mode, thereby modifying phase matching with the cavity mode. For very narrow waveguides ($w = 10,20$ nm) the mode is extremely confined and lossy, producing strong impedance mismatch and distorted, broadened spectra. For $w \geq 30$ nm, the effective index saturates, yielding nearly identical coupling conditions and thus almost overlapping transmission responses. Among the investigated cases, the minimum FWHM is obtained at $w = 80$ nm, which is therefore selected as the optimal waveguide width for the subsequent analysis. The reduced FWHM at this configuration enhances ER, making it the most suitable structure for high-performance sensing applications.

The next investigated parameter is the coupling gap (g) between the waveguide and the cavity. After fixing the optimized waveguide width and other structural parameters, g was varied from 5 nm to 25 nm in steps of 5 nm, as shown in Fig. 6. The results reveal pronounced effects on both the resonance wavelength and the FWHM. The gap g between the MIM waveguide and the semi-rectangular cavity directly controls the evanescent coupling strength and hence the external coupling rate γ_e. For small gaps, strong overlap of the gap-plasmon field with the

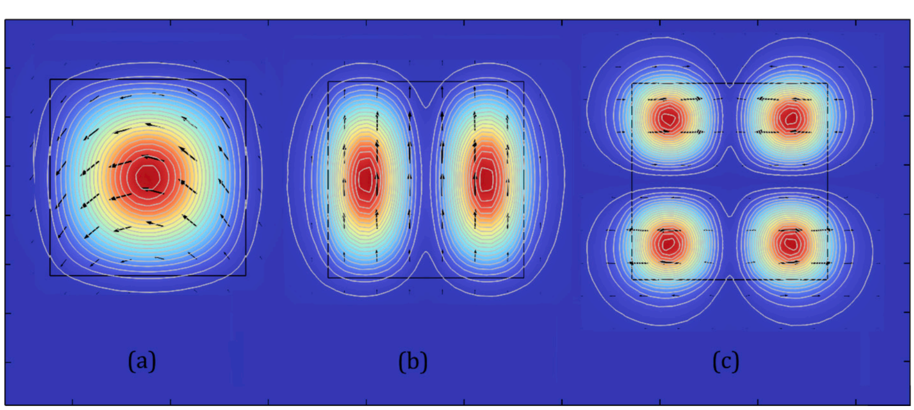

Fig. 4. Field intensity and power flux diagrams of the fundamental and higher order modes of the waveguide.

cavity mode leads to an over-coupled regime with a relatively broad but deep resonance. As g increases, γ_e decreases approximately exponentially and becomes comparable to the intrinsic loss γ_i, bringing the system close to critical coupling, where the transmission dip is maximized. Further increase of g drives the device into an under-coupled regime: only limited power is transferred to the cavity, so the resonance becomes weaker and broader. In this regime, the reduced hybridization lowers the effective index of the coupled mode, so the Fabry–Perot condition is satisfied at shorter wavelengths, producing the observed blue shift. Specifically, increasing the gap leads to a blue shift of the resonance wavelength and a reduction in FWHM, while simultaneously decreasing the transmittance signal intensity due to weaker coupling strength. Considering the trade-off between resonance sharpness and signal intensity, g = 15 nm is identified as the optimal gap distance for subsequent analyses.

It should be noticed that fabrication variation of the coupling gap g would affect performance. For example, reducing g to ~10 nm increases plasmonic coupling, causing a slight redshift of the resonance and somewhat higher sensitivity, but with broader linewidth (lower Q) due to enhanced metal loss. Conversely, increasing g to ~20 nm weakens coupling, leading to a modest blueshift and reduced sensitivity with a higher Q. Our test simulations suggest only a few nanometer shift in peak wavelength for a ± 5 nm gap change. Another key design variable is the length l of the semi-rectangular cavity. Fig. 7 shows the transmission spectra for l varying from 96 nm to 672 nm in steps of 96 nm. The semi-rectangular branch behaves as a Fabry–Perot type plasmonic cavity, so its resonances approximately satisfy $2n_{eff}L = m\lambda$. Consequently, increasing l enlarges the optical path length and shifts the resonance condition to longer wavelengths, producing the observed sequence of red-shifted dips. When l becomes sufficiently long, higher-order longitudinal modes (larger m) also fall inside the considered wavelength window, which explains the appearance of additional resonance minima. However, longer cavities also imply a greater propagation distance in the metallic region and therefore larger intrinsic loss, leading to broader FWHM and reduced quality factor. A length of l = 384 nm offers the best compromise, providing a deep resonance with a FWHM of 27.5 nm while keeping the resonator footprint and loss at acceptable levels.

The last optimized structural parameter is the separation distance (d) between the two coupled semi-rectangular resonators. The parameter (d) controls the near-field coupling between the two cavity arms and consequently their hybrid super modes. As shown in Fig. 8, d was varied from 10 nm to 60 nm in steps of 10 nm. The results show that for small separations (d ≤ 20 nm), the strong interaction leads to a significant mode splitting into symmetric and antisymmetric branches, which causes an additional shallow depression of about 1.35 μm and a modified main resonance. In other words, a strong near-field coupling occurs between the resonators, which significantly affects the resonance wavelength and FWHM. However, when the distance exceeds 20 nm, the coupling strength decreases rapidly due to the exponential decay of the unstable plasmonic field, and further increase of d no longer affects the transmission spectrum, and the modes degenerate again, and the spectra converge to a single, stable resonance. Since the case of d = 10 nm shows relatively weak transmission intensity, while d = 20 nm provides sufficient coupling and stable FWHM, d = 20 nm is identified as the optimal distance between the two resonators.

In order to investigate and clarify why the distance d between the cavity arms is an optimal value, the electric field profiles at the resonance wavelength for different d are compared in Fig. 9. As can be seen, for d = 10 nm, the two arms are strongly coupled, and the resonant field is mainly concentrated in the very narrow gap between them and in the adjacent corners. This strongly hybridized super mode stores a significant part of its energy in the metal-metal gap, so the effective $\int |E|^2 dV$ (Analyte) with the analyte is not maximized, the resonance becomes broader and weaker. However, when d = 20 nm, the coupling between the arms is modulated, and the cavity supports a fundamental Fabry-Perot-like mode with a single lobe that fills most of the semi-rectangular channel. Here, the electric field remains high along the entire path filled with analyte, which provides a large mode overlap coefficient and results in the highest sensitivity and FOM. Also, for d = 30 nm and larger, the field pattern is still dominated by this fundamental mode, but the intensity in the analyte region decreases slightly and is scattered into the surrounding dielectric, so the overlap gain saturates while the intrinsic losses increase. Therefore, the optimal d is obtained from a balance between sufficient inter-arm coupling and maximum field overlap with the analyte.

It should be noted that in practice, fabrication imperfections mainly appear as small deviations in the coupling gap g, waveguide width w, cavity length l, and inter-arm spacing d. The parametric sweeps presented in Fig. 5 up to Fig. 8 already provide a practical tolerance analysis for these quantities. Around the chosen optimum, the resonance wavelength and FOM vary smoothly with geometry, and dimensional changes on the order of ±5–10 nm lead only to minor calibration shifts rather than drastic degradation of the resonance depth or sensitivity, indicating good robustness to realistic fabrication errors.

For the optimized sensor, the H-field mapping in the sensor device at the resonance and non-resonance wavelength, which is shown in Fig. 10 (a), and Fig. 10(b), respectively. It can be realized that at the resonance wavelength (λ = 1432.4 nm), the H-field becomes concentrated in the resonator cavities with the max field values in L = 600.00 nm, W = 415.00 nm, is equal to |H| = 1225.05 A/m, whereas at the non-resonant wavelength (λ = 915.79 nm) the H-field remains confined to the main waveguide, and the max field values is |H| = 257.40 V/m in L = 380.00 nm, W = 115.00 nm. This is explained by the coupling theory between the resonator and the waveguide. When the input frequency matches the cavity resonance, the energy enters the resonator. It means when the waveguide mode is phase-matched to the cavity mode, electromagnetic energy is transferred into the cavities, but in the non-resonant wavelength, the fields remain confined to the main waveguide. Also, the electric field distribution (*E*-field), which is more directly related to the sensing volume and light-matter interaction, is shown in Fig. 10(c) and Fig. 10(d). It can be observed that at the resonance wavelength (λ = 1432.4 nm), the electric field is strongly concentrated inside the semi-rectangular cavity, with a maximum value of $|E| = 6.5064 \times 10^5$ V/m at *L*=775 nm, *W*=385 nm. In contrast, at the non-resonant wavelength (λ = 915.79 nm), the field remains mainly confined to the MIM bus waveguide, and the maximum value is only $|E| = 9.8707 \times 10^3$ V/m at L = 472.57 nm, W = 165.07 nm. This behavior follows directly from waveguide–cavity coupling theory: when the input wavelength is phase-matched to the cavity eigenmode, energy is efficiently transferred from the TM_{00} bus mode into the cavity and stored there, while at off-

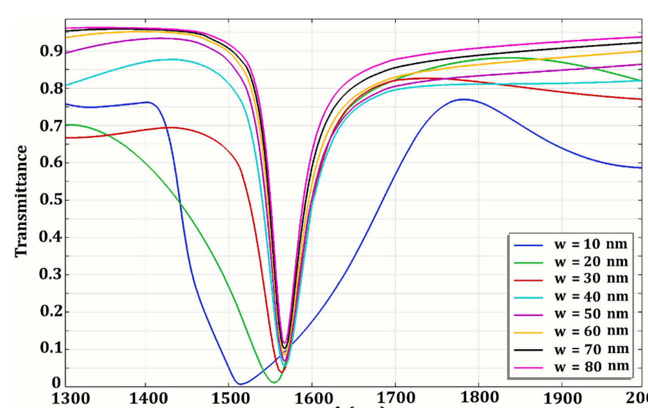

Fig. 5. Transmission spectra of the proposed sensor for different values of waveguide width (w), showing the effect of w variation on the resonance wavelength.

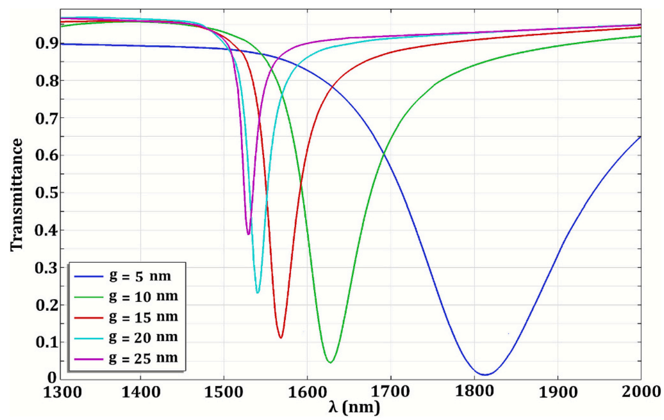

Fig. 6. Transmission spectra of the proposed sensor for different gap values (g), showing the effect of g variation on the resonance wavelength.

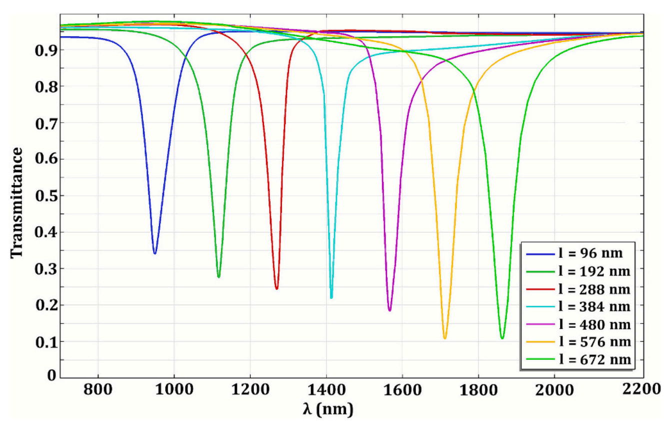

Fig. 7. Transmission spectra of the proposed sensor for different values of coupled semi-rectangular resonator (l), showing the effect of l variation on the resonance wavelength.

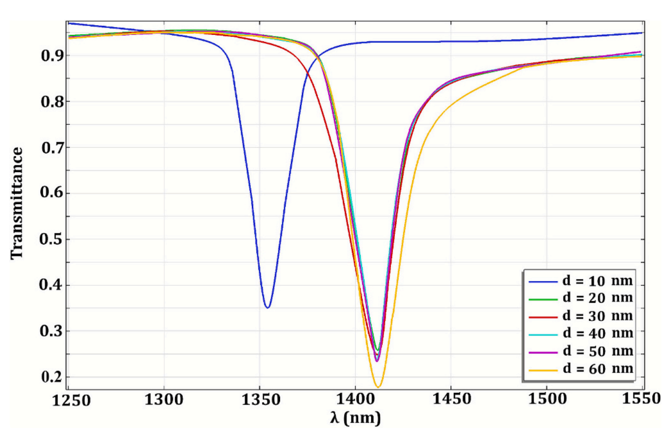

Fig. 8. Transmission spectra of the proposed sensor for different values of distance between two coupled semi-rectangular resonators (d), showing the effect of d variation on the resonance wavelength.

resonant wavelengths the phase mismatch prevents efficient coupling and the electromagnetic energy continues to propagate along the main waveguide with only weak penetration into the cavity region.

It should be noted that at the resonance wavelength, the H–field is strongly confined inside the semi-rectangular cavity, indicating that a large fraction of the modal energy resides in the analyte region rather than in the metal. According to perturbative resonance theory, the wavelength shift induced by a refractive-index change scales with this energy-overlap factor. Consequently, the intense, localized field in the cavity maximizes the effective interaction length with the analyte and directly underpins the high RI sensitivity achieved by the proposed sensor.

To elucidate the sensing mechanism, we analyze the electric and magnetic field distributions in the optimized structure. At the resonant wavelength, the electric field norm with a very high peak is strongly concentrated inside the semi-rectangular cavity and near the inner corners of the cavity arms. These hot spots originate from the surface charge accumulation at the metal-dielectric discontinuities and indicate a strong confinement of the plasmonic mode in the analyte-filled region. In contrast, at the non-resonant wavelength, the field remains mainly in the MIM passage waveguide, with only weak penetration into the cavity. Therefore, the energy density in the sensor volume increases by more than an order of magnitude at resonance. The corresponding E and H field patterns also show a single lobe without any internal nodes, confirming the excitation of the Fabry-Pérot cavity mode, a fundamental dipole-like structure underlying the large resonance displacements.

In this work the charge-density maps are not computed, but prior studies have shown their value in identifying mode character. For example, [60] mapped induced surface charges in closely related MIM-like nanorod structures and showed that the pattern of positive/negative charges directly distinguishes simple dipolar SPP modes from hybrid cavity (core) plasmon modes. By analogy, the observed resonance in this work arises from strong hybridization of the side-cavity and waveguide modes. The observed resonance behavior can be interpreted through coupled-mode theory, where energy is transferred between the waveguide and cavity when their modes are phase-matched. Changes in coupling gap or surrounding refractive index perturb this interaction, wider gaps weaken coupling (blue-shift), while increased index red-shifts the resonance due to an effectively longer optical path, as predicted by perturbation theory. These trends are consistent with established models and prior studies such as [61].

3.4. *Sensitivity testing of PSA biosensor*

After fine-tuning the structural characteristics of the proposed MIM plasmonic sensor, its performance was evaluated in a practical biosensing scenario, namely the detection of PSA. PSA is a well-established biomarker for PC, and its early and precise detection is essential for accurate diagnosis and effective clinical monitoring. In this context, the optimized sensor geometry was exposed to variations in the refractive index of the surrounding analyte medium, which mimicked different PSA concentrations. The sensitivity of the proposed sensor is evaluated by monitoring the resonance wavelength shift as a function of the refractive index variations induced by different PSA concentrations. This plasmonic sensing mechanism is inherently label-free and capable of providing real-time detection, which significantly improves upon conventional diagnostic approaches such as ELISA and PCR. While these techniques remain the clinical gold standards due to their specificity, they suffer from important limitations, including long assay times, labor-intensive protocols, and dependence on costly laboratory infrastructure [62,63]. In contrast, MIM plasmonic biosensors exploit strong electromagnetic field confinement within the nanoscale dielectric gap, which maximizes light–matter interaction at the sensing interface [51,64]. This unique property enables the detection of subtle refractive index changes caused by PSA binding events, resulting in high sensitivity and low detection limits. Moreover, the planar and compact geometry of MIM structures facilitates seamless integration with microfluidic platforms and on-chip optical components, paving the way for portable, point-of-care diagnostic devices [65]. Compared to single-interface SPR sensors, MIM configurations achieve narrower resonance linewidths and enhanced figures of merit, making them particularly well-suited for detecting clinically relevant biomarkers, such as PSA [66,67].

The simulated MIM plasmonic sensor exhibits a pronounced SPR dip

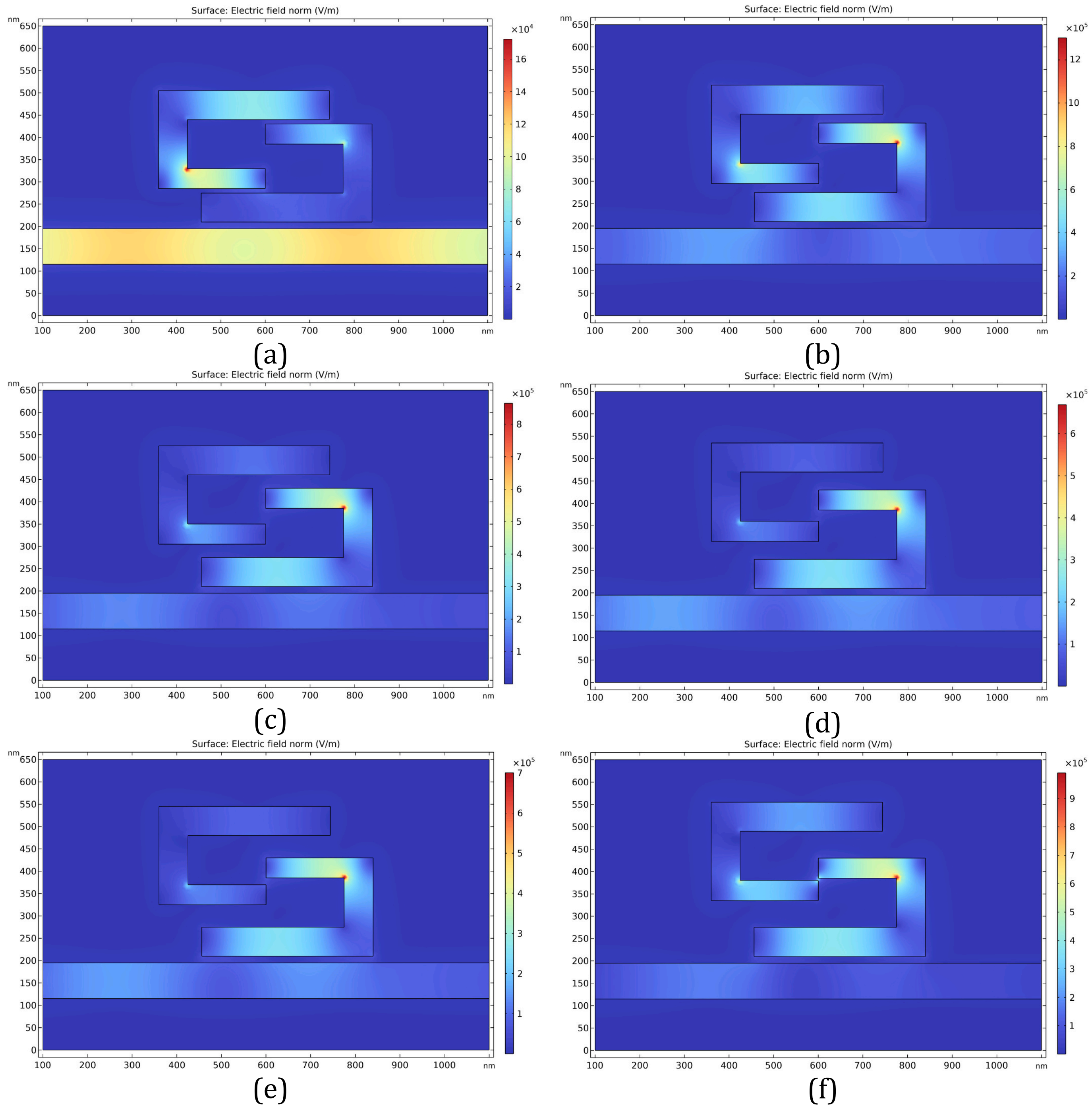

Fig. 9. Electric field distribution profile for different values of d; (a) d = 10 nm, (b) d = 20 nm, (c) d = 30 nm, (d) d = 40 nm, (e) d = 50 nm, (f) d = 60 nm.

whose center wavelength shifts strongly with PSA concentration, as shown in Fig. 11. As the PSA analyte increases from zero to C = 500 (arbitrary units), the resonance redshifts from 1432.4 nm to 1526.4 nm, nearly linearly with concentration. A linear fit yields ~0.19 nm shift per concentration unit. Extrapolating to refractive index units, this implies a bulk sensitivity on the order of 1872.25 nm/RIU, comparable to state-of-the-art plasmonic refractometers. The nearly linear redshift confirms the expected SPR sensing mechanism: PSA binding increases the local dielectric index, shifting the MIM resonance to longer wavelengths [68]. Importantly, the resonance linewidth or FWHM remains essentially constant at 24 nm across all PSA levels (only growing from 24.0 to 24.8 nm at the highest loading). This stable, narrow FWHM indicates that the mode's QF is preserved even as analyte accumulates, implying a high figure-of-merit 76.6 RIU^{-1} for detecting small index changes and high-quality resonances with a high Q-factor 60.3. For this configuration, the LoD is obtained as 0.0108 RIU.

3.5. *Validation of sensor linearity across a broad refractive index range*

In this section, to prove the assumed linear response of the proposed sensor, an additional parametric study is performed over a wider refractive index range. The transmission spectra for analyte indices from 1.30 to 1.40 are recalculated, and the corresponding resonance wavelengths are systematically extracted. The resulting multi-index transmission curves are presented along with a plot of resonance wavelength versus refractive index, and the linearity is quantified using sensitivity,

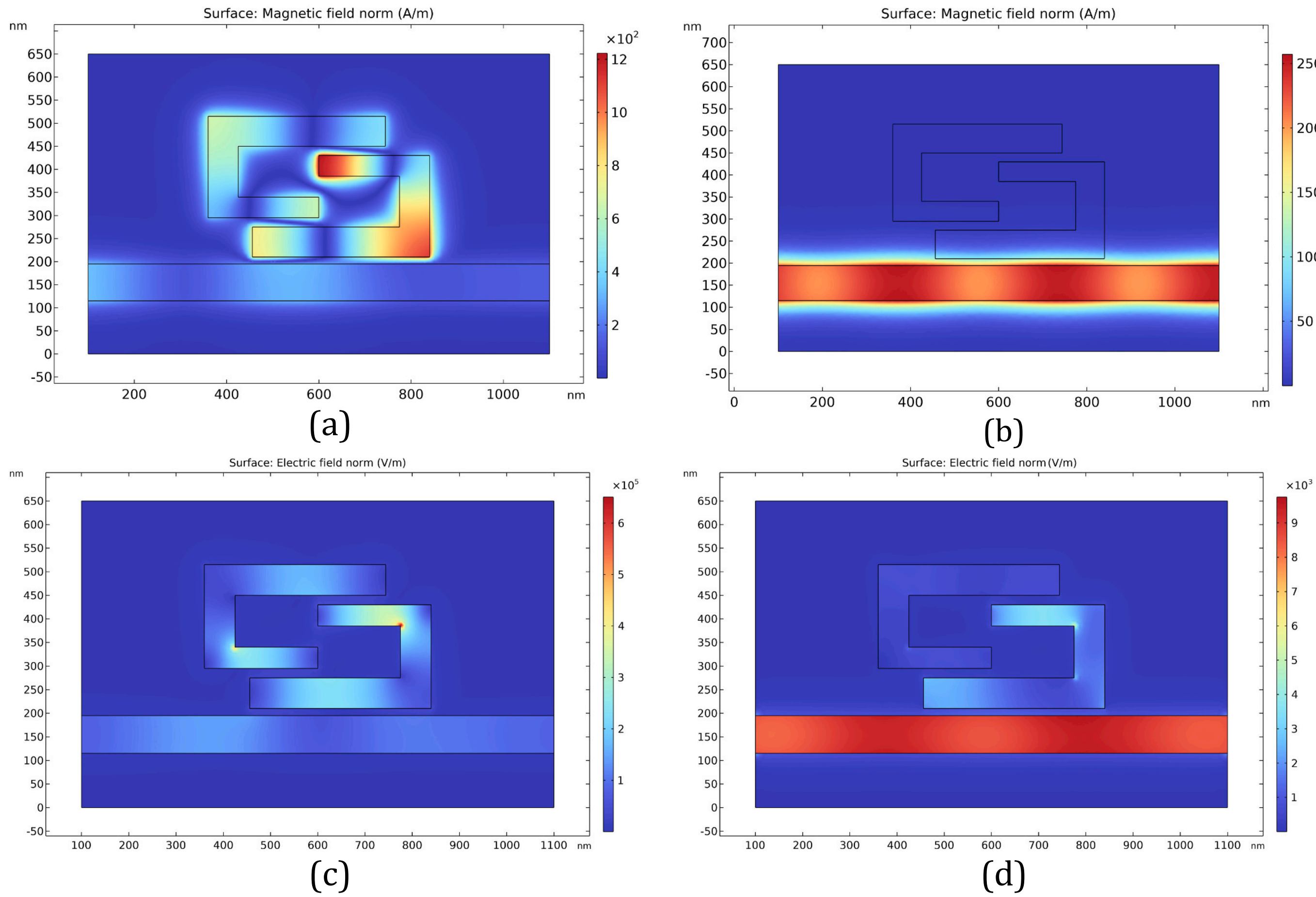

Fig. 10. H-field mapping in the optimized sensor at (a) 1432.4 nm, (b) 915.79 nm; E-field mapping in the optimized sensor at (c) 1432.4 nm, (d) 915.79 nm.

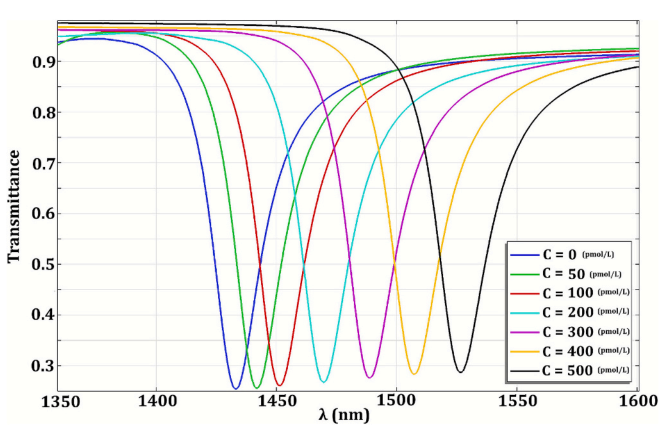

Fig. 11. Transmission spectra of the optimized MIM plasmonic biosensor under varying PSA concentrations (C = 0 pmol/L to 500 pmol/L).

R^2, RMSE, and nonlinearity error. Fig. 12(a) shows the calculated transmission spectra of the sensor for several sample refractive indices in the range of interest ($n = 1.30$–1.40). For each refractive index, a single, well-defined resonant dip is observed, whose spectral position gradually shifts towards longer wavelengths with increasing n, while the overall spectral shape and minimum transmission loss remain almost unchanged. The absence of additional parasitic losses or significant distortions in the resonance profile indicates that the main guided mode is preserved and only its effective refractive index is modified by the analyte. This behavior indicates a robust and reproducible resonance mechanism that ensures that the resonance wavelength can be reliably tracked as a function of refractive index, which is essential for high-precision and calibration-compatible refractive index sensing. Also shown in Fig. 12(b) is the dependence of the resonance wavelength on the refractive index of the analyte in the range 1.30 to 1.40. The resonance wavelengths for each refractive index are indicated in this figure, and the least squares linear fit is shown on it. With increasing refractive index, a completely uniform red shift of the resonance is observed from ≈1400 nm to ≈1510 nm, indicating a good dispersion response of the sensing mode. The fitted slope shows an average sensitivity of 1060.71 nm per measurement unit. The goodness-of-fit indices, $R^2 = 0.999944$ and RMSE = 0.2723 nm, together with a very small nonlinear error of 0.3414 %, confirm that the deviation from ideal linearity is negligible and justify the use of a single constant sensitivity for this RI range.

In the following section, a comparative analysis is performed to further demonstrate the effectiveness of the proposed structure, using a simple rectangular resonator geometry as the baseline configuration. This comparison enables the contribution of the added structural features to be clearly isolated, allowing for an assessment of how each modification improves the resonance behavior, sensing performance, and spectral stability. By comparing both designs under the same simulation conditions, the improvements resulting from the optimized configuration are quantitatively revealed.

In Fig. 13, the transmission spectra of the reference rectangular cavity (base) and the proposed semi-rectangular resonator at ($n = 1.30$) and ($n = 1.32$) are compared. Both structures exhibit a single resonant attenuation, but its evolution with refractive index is clearly different. As is clear, the proposed resonator produces a deeper and more spectrally pronounced attenuation band with a more pronounced red shift

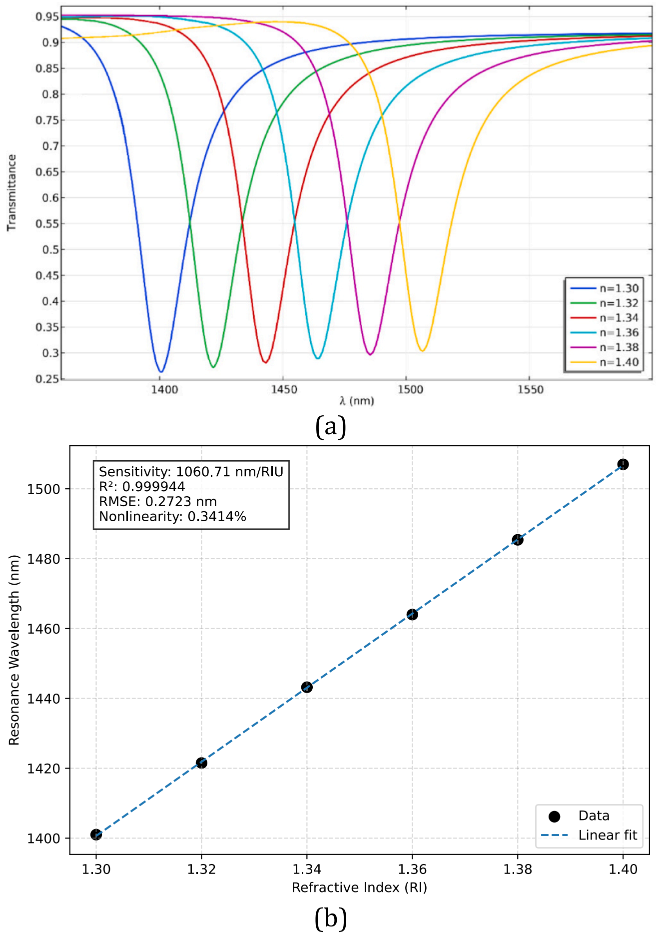

Fig. 12. (a) Transmission spectra for multiple refractive indices; (b) Resonance wavelength versus refractive index with linear regression fit.

from the minimum as (n) increases, indicating stronger field-analyte overlap and higher spectral sensitivity. The calculated values for the sensor performance parameters in this case are:

S = 1025 nm/RIU, FWHM = 23.3 nm, QF = 60.48, and FOM = 43.61 RIU^{-1}. In contrast, the rectangular base cavity shows a broader and shallower resonance with a smaller wavelength shift, indicating a weaker confinement in the sensing region and, consequently, a lower refractive index sensitivity, and the FWHM is twice that of the proposed case. The values obtained in this case are also: S = 967 nm/RIU, FWHM = 42.1 nm, QF = 36.4, and FOM = 26.1 RIU^{-1}.

Also, in Fig. 14, a general attempt has been made to compare the structures based on the electric and magnetic field profiles. In this regard, in Fig. 14(a) and 14(b), the electric and magnetic field profiles for the basic structure are shown. The maximum magnitudes of these fields were obtained as 160 A/m and 12E3 V/m in the basic structure, respectively. The values obtained for these parameters and for the proposed structure are much larger than the base structure. For the proposed structure and under similar conditions, values of 1226.51 A/m and 5.2326E5 V/m for the magnetic and electric fields at the resonance wavelength were obtained. This shows that the semi-rectangular resonator provides stronger field confinement and larger overlap between the guided mode and the analyte volume. Thus, the light-matter interaction is enhanced, which directly results in a larger resonance wavelength shift and improved sensitivity and FOM. Also, the more localized fields indicate more efficient coupling between the waveguide and the resonator, so the geometry is not just an appearance modification, but is physically superior in focusing the optical energy where sensing occurs.

Since for any practical application of a biosensor, the evaluation of its thermal stability is a vital issue, so in Fig. 15, the response of the sensor and its sensitivity for temperatures between 263.15 K and 313.15 K have been examined. In this range of 50 K, the resonance wavelength shows only an average red shift of ≈2.8 nm in total, while the resonance depth and linewidth remain almost the same. The corresponding refractive index sensitivity, evaluated between 1.3300 and 1.3388, ranges from 1085 nm/RIU at the lowest temperature to 1096 nm/RIU at the highest temperature, compared to 1091 nm/RIU at the nominal state. Therefore, both the resonance position and the sensitivity change by less than about ±0.5 %, indicating that the proposed semi-rectangular cavity is inherently tolerant to real temperature fluctuations. Additionally, any residual drift can be easily compensated using a standard temperature stabilizer or on-chip reference channels.

3.6. Comprehensive comparison with previous works

Table 4 summarizes the reported performance metrics of representative MIM-based plasmonic sensors in comparison with our design. [10] presents a dual-ring resonator coupled to a MIM waveguide for the

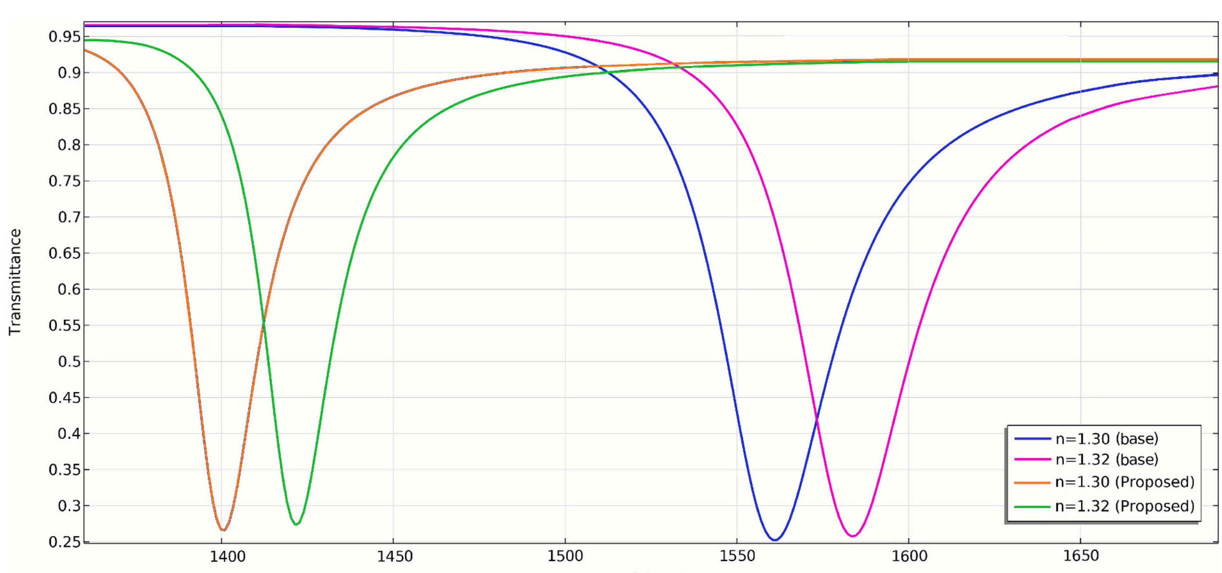

Fig. 13. Transmission spectrum for the basic and proposed structure.

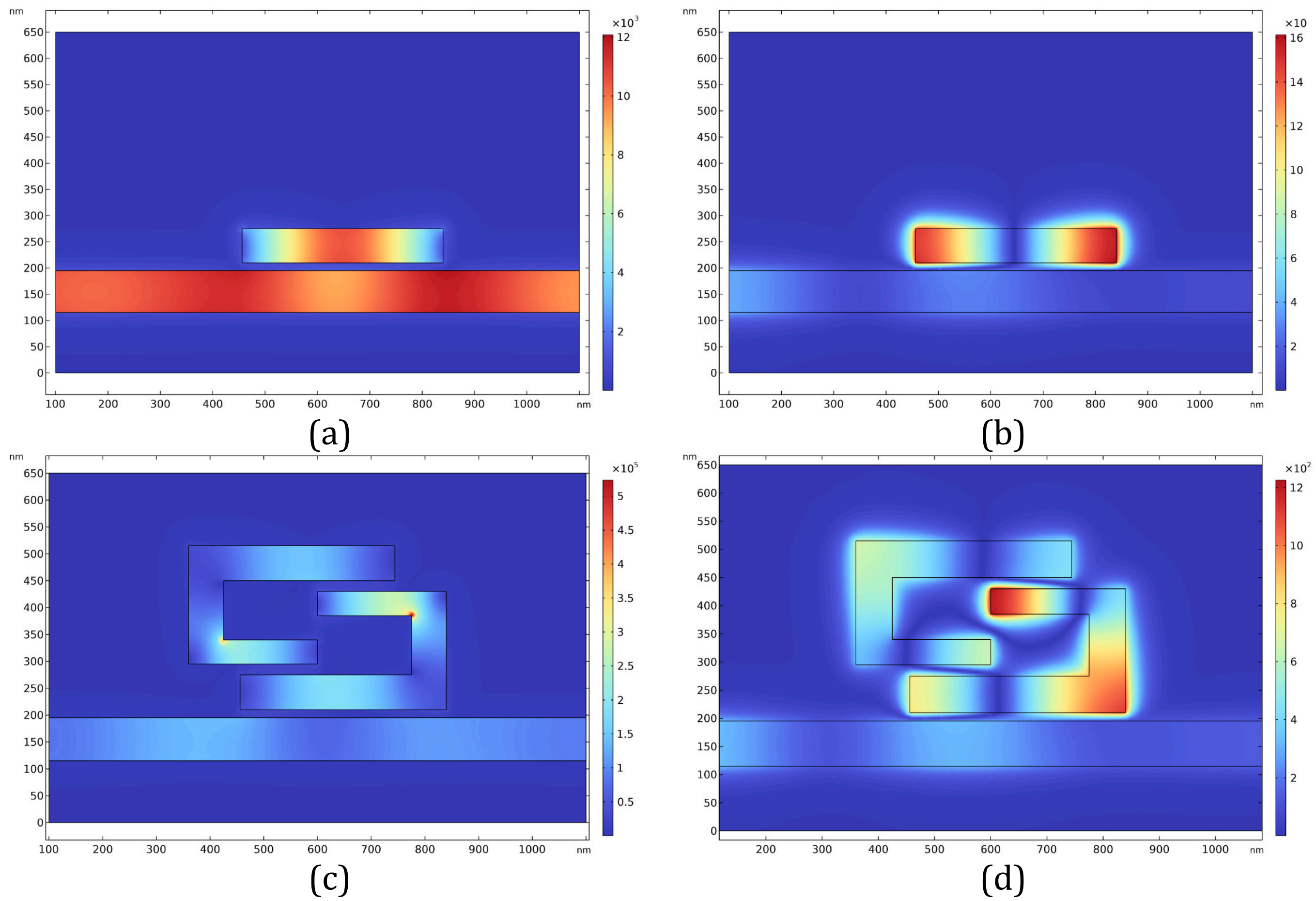

Fig. 14. (a) Electric field, and (b) Magnetic field distribution profile of the basic structure at the resonance wavelength of 1534.9 nm; (c) Electric field, and (d) Magnetic field distribution profile of the basic structure at the resonance wavelength of 1421.5 nm.

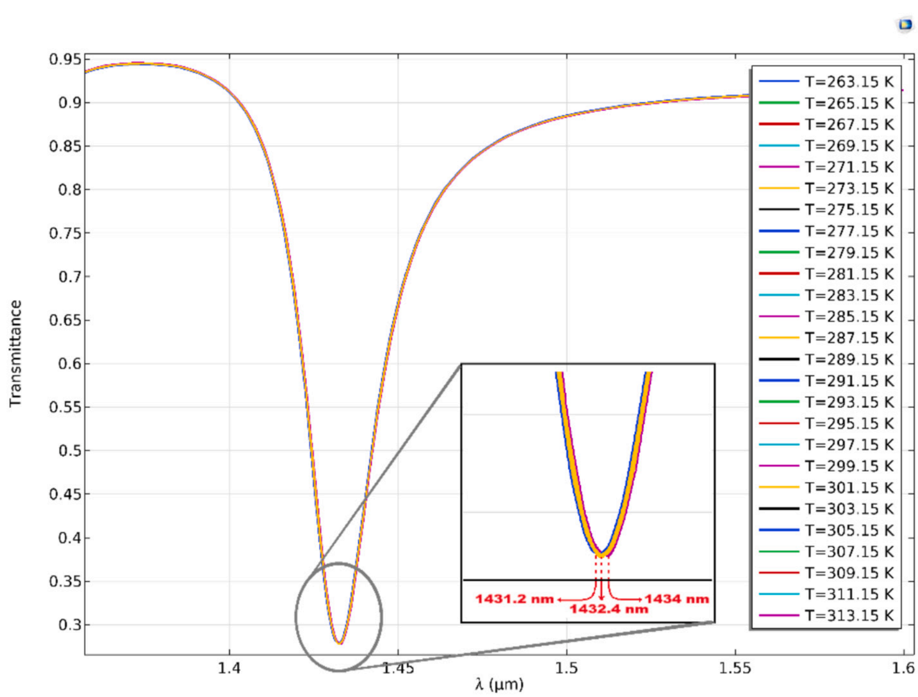

Fig. 15. Effects of temperature change on the transmission spectrum.

detection of various bacterial pathogens yielded a sensitivity of ≈324.76 nm/RIU and a FOM of 10.187. In [37], Ag nanoring and disk resonators were investigated for PSA detection, where the Ag nanoring achieved a sensitivity of ≈567 nm/RIU with a FOM of ≈3.72. An 8-shaped MIM resonator to detect basal cancer cells was reported in [69], demonstrating a sensitivity of ≈1200 nm/RIU and an ultrahigh QF of ≈250. A recent multi-mode ring supercell sensor targeting cancer biomarkers (carcinoembryonic antigen, PSA, and hemoglobin) [70] attained a sensitivity of ≈913.5 nm/RIU with FOM >70. In [71], an L-shaped resonator side-coupled to a MIM waveguide to detect Alcohol, achieved a sensitivity of ≈1638 nm/RIU. A rectangular hollow MIM structure for the detection of tuberculosis (TB)-infected blood plasma was proposed in [72], reaching a sensitivity of ≈900 nm/RIU with a FOM of 11.84. More recently, an enhanced MIM sensor integrating graphene, silver, and magnesium fluoride for early-stage blood cancer detection [73] demonstrated a sensitivity of ≈1428 nm/RIU. A refractive index MIM sensor with U-shaped and inverted U-shaped resonators achieved a sensitivity and FOM of 571.4 nm/RIU, and 14,987, respectively [74]. One-dimensional photonic crystal lattices coupled to two MIM waveguides designed for the detection of basal cell cancer [75], obtained sensitivities and FOM as 718.6, 714.3 nm/RIU, and 156.217, 60.1, respectively. In [76], a MIM-based sensor incorporating an elliptical resonator was designed, achieving a sensitivity of up to 550 nm/RIU and a FOM of 282.5. In contrast, the proposed sensor in this work exhibits substantially higher sensitivity, while maintaining a narrow FWHM. Our designed achieves very high sensitivity together with a relatively narrow FWHM, offering a strong FOM, while other MIM geometries often reach extreme FOM or Q-factor only by sacrificing sensitivity or, conversely, achieve high sensitivity with much broader resonances. MIM-based biosensors have been practically applied in several real-world contexts, demonstrating their feasibility beyond theoretical designs. For example, MIM structures have been used for label-free detection of biomolecular interactions by enabling analytes to access plasmonic hotspots in accessible nanogap regions [77]. In another demonstration, a flexible MIM nanodisk array on a PDMS substrate was fabricated and experimentally employed for the detection of A549 lung cancer cells, achieving a sensitivity of ∼1500 nm/RIU and maintaining performance under mechanical bending, thereby highlighting the potential of MIM designs for practical, wearable biosensing applications [78]. More recently, nanocup-shaped MIM structures composed of Au–TiO_2–Au layers have been fabricated and applied for spectrometer-free biosensing, enabling label-free detection of the clinically relevant biomarker Carcinoembryonic Antigen (CEA) with a limit of detection around 10 ng/mL, thus demonstrating the capability of MIM biosensors for point-of-care diagnostics [79]. While simulation-based studies of MIM biosensors provide valuable insights into optimizing structural parameters and predicting performance, they often neglect fabrication tolerances, surface chemistry, and the complex behavior of biological samples. As a result, simulated designs may not fully capture the real-world sensing performance, highlighting the need for experimental validation.

Table 4
Performance metrics comparison of representative MIM sensors to our design.

Sensor Structure	Sensitivity (nm/RIU)	FWHM (nm)	FOM (RIU^{-1})	Ref.
Dual-ring MIM resonator	324.76	31.88	10.187	[16]
Ag nanoring MIM sensor	567.2	152.47	3.72	[37]
8-shaped MIM resonator	1200.0	∼4.8	250	[69]
Ring-resonator supercell	913.5	13.05	>70.0	[70]
L-shaped MIM resonator	1638	75	21.84	[71]
Rectangular hollow MIM resonator	900	76.01	11.84	[72]
Phi-Configured Graphene-Enhanced MIM sensor	1428	19.83	72	[73]
U-shaped and inverted U-shaped resonators	571.4	0.038	14,987	[74]
One-dimensional photonic crystal lattices coupled to two MIM waveguides	718.6, 714.3	4.6, 11.88	156.217, 60.1	[75]
elliptical resonator	550	1.94	282.5	[76]
This work	1872.3	24	76.6	–

Across the cited works in the comparison table, several potential disadvantages can be identified when one moves from purely numerical metrics to practical implementation. Many of the designs (e.g., nano wall-modified bowties, figure-of-8 cavities, ring-resonator supercells) rely on intricate multi-gap or multi-resonator geometries that demand high-resolution lithography, strict alignment, and uniformity over large areas; their predicted high Q and FOM values are therefore sensitive to fabrication tolerances, edge roughness and dimensional drift. Very high-Q resonances are also intrinsically narrowband, which makes them vulnerable to spectral drift under temperature, contamination, or index fluctuations and can complicate read-out in realistic biochemical environments. Some structures operate at longer wavelengths or require specific illumination and polarization conditions, limiting compatibility with compact telecom-band, fiber-coupled or on-chip interrogation schemes. In addition, multi-resonant or strongly polarization-dependent responses, while attractive for multiplexing, can make calibration less straightforward and reduce robustness to angular or polarization variations. Compared with simpler single-stub or single-ring MIM resonators, these elaborate configurations usually have larger footprints, more coupled design parameters and higher fabrication cost, and the performance advantage may diminish once these practical constraints are considered. However, the design presented in this paper simultaneously provides high sensitivity (1872.3 nm/RIU), narrow FWHM (24 nm), high FOM (76.6 RIU^{-1}) and respectable Q-factor (60.3) in the telecom near-infrared band, while maintaining a nearly linear response even at higher refractive indices. In contrast, figure-8 and supercell resonators that achieve very high Q or similar FOM rely on complex multi-slot or multi-resonator layouts that are more construction-sensitive and sensitive to dimensional tolerances. Likewise, nano wall-modified bowties and other highly sensitive designs often target different spectral ranges or require more demanding nanolithography. Using a relatively compact, two-cavity semi-rectangular geometry designed expressly for the PSA refractive index window in aqueous media and compatible with nanoimprint lithography, our sensor offers a balanced, application-based trade-off that is particularly suitable for integrated PSA and point-of-care.

The present work, along with the potential benefits it has provided, also includes a series of limitations. The basis of this study was based on numerical analysis considering practical conditions. Because currently, there is no access to a clean room and nanofabrication facilities that are able to reliably produce the sub-wavelength features required by the proposed structure. On the other hand, experimental validation is also limited by the lack of high-resolution optical characterization equipment (e.g., tunable narrow-linewidth lasers and spectrum analyzers with good resolution) and the high cost of these devices, which are required to accurately measure the Q-factor and FOM at the designed wavelengths. It should be noted that the present numerical analysis considers uniform bulk refractive index variations in the sensing region, which is the standard figure of merit for evaluating plasmonic sensor platforms. In a practical PSA assay, the metal surface would be functionalized with a thin biorecognition layer, for example, a thiolated self-assembled monolayer, followed by covalent immobilization of anti PSA antibodies and subsequent blocking to suppress non-specific adsorption. The thin biochemical film and specifically bound PSA molecules effectively modify the local refractive index sampled by the confined mode, so the high bulk sensitivity reported here directly translates into strong responsivity to such nm scale biolayers. Therefore, in this study, due to the lack of facilities to host a dedicated biolab for working with PSA, surface functionalization and clinical assay preparation are not available, and biomolecular effects are demonstrated through equivalent refractive index changes. Finally, advanced packaging and fiber-to-chip connection configurations are not available within the framework of the current project. Therefore, future work could focus on system-level integration as a natural continuation of this work in collaboration with specialized laboratories.

4. Conclusion

In this work, a novel plasmonic biosensor is proposed and systematically investigated, which consists of a pair of semi-rectangular resonators coupled to a MIM waveguide. The device exploits strong waveguide–resonator coupling at the resonance wavelength, enabling efficient field confinement and enhanced light–matter interaction, which in turn improves sensitivity to refractive index variations and facilitates precise detection of biomolecular binding events. Through rigorous optimization of the structural parameters, specifically the waveguide width(w), the distance between the resonator and waveguide (g), resonator length (l), and the distance between two semi-rectangular resonators (d), the sensor was tailored for high-performance operation in the detection of PSA, as one of the most commonly diagnosed cancers among men. The optimized biosensor demonstrates excellent performance metrics, including a sensitivity of 1872.3 nm/RIU, a narrow FWHM of 24 nm, a high FOM of 76.6 RIU^{-1}, a QF of 60.3, and a LoD of 0.0108 RIU, through examining different PSA concentrations. These values surpass those of many previously reported MIM-based PSA sensors, confirming the advantage of the proposed geometry in achieving both high sensitivity and spectral sharpness. The designed biosensor is compatible with established nanofabrication methods, underscoring its practical feasibility and paving the way for straightforward experimental realization and potential integration into real-world sensing applications. Collectively, these results demonstrate the potential of the proposed sensor as an effective platform for real-time, label-free PSA detection. However, there is still work to be done to develop this field of science. Future research could focus on integrating plasmonic sensors with microfluidic and portable platforms to enable rapid, in situ detection. Also, the development and optimization of scalable fabrication processes, such as nanoimprint lithography, will pave the way for commercialization and widespread use of this technology.

CRediT authorship contribution statement

Asghar Molaei-Yeznabad: Writing – review & editing, Visualization, Validation, Resources, Methodology, Investigation, Formal analysis, Data curation, Conceptualization. **Hamid Bahador:** Writing – review & editing, Visualization, Validation, Supervision, Resources, Methodology, Formal analysis, Conceptualization. **Ghazal Abdi:** Writing – review & editing, Writing – original draft, Visualization, Resources, Methodology, Investigation. **Azadeh Nilghaz:** Writing – review & editing, Validation, Supervision, Software.

Funding

No funding was received for conducting this research.

Declaration of competing interest

The authors declare that they have no known competing financial interests or personal relationships that could have appeared to influence the work reported in this paper.

Data availability

The data that support the findings of this study are available from the corresponding author upon reasonable request.

References

[1] A. Hunt, G. Slaughter, Electrochemical detection of prostate cancer-associated miRNA-141 using a low-cost disposable biosensor, Biosensors (Basel) 15 (6) (2025).
[2] S.-T. Pang, et al., Urinary MicroRNA-21 for prostate cancer detection using a silver nanoparticle sensor: a promising diagnostic tool, Biosensors 14 (12) (2024) 599.
[3] A. Ramola, A.K. Shakya, A. Bergman, Comprehensive analysis of advancement in optical biosensing techniques for early detection of cancerous cells, Biosensors 15 (5) (2025) 292.
[4] M. Sadeghi, et al., A comprehensive review on electrochemical nano biosensors for precise detection of blood-based oncomarkers in breast cancer, Biosensors 13 (4) (2023) 481.
[5] A. Molaei-Yeznabad, H. Bahador, Refractive index-based optimized ternary photonic crystal biosensor for ultra precise detection of cancer cells, Sensing Imaging 26 (1) (2025) 36.
[6] F. Chen, et al., Temperature tunable Fano resonance based on ring resonator side coupled with a MIM waveguide, Opt. Laser Technol. 116 (2019) 293–299.
[7] L. Singh, et al., Plasmonic MIM waveguide based FR sensors for refractive index sensing of human hemoglobin, Photonics Nanostruct. Fundam. Appl. 62 (2024) 101325.
[8] G. Abdi, H. Bahador, High sensitivity and optimum design of LSPR-based sensors by coupled nano-rings for cancer detection, Opt. Lasers Eng. 174 (2024) 107975.
[9] H. Kurt, et al., Rapid and sensitive biosensing of uropathogenic *E. coli* using plasmonic nanohole arrays on MIM: bridging the gap between lab and clinical diagnostics, Biosens. Bioelectron. 280 (2025) 117419.
[10] L. Singh, et al., MIM waveguide based multi-functional plasmonic logic device by phase modulation, IEEE Trans. Nanotechnol. 23 (2024) 368–375.
[11] C. Tang, et al., Enhanced light absorption of graphene sheet with large bandwidth tunability in visible and near-infrared range, Phys. Lett. A 555 (2025) 130791.
[12] C. Tang, et al., Ultra-broadband near-infrared absorption enhancement of monolayer graphene by multiple-resonator approach, Diam. Relat. Mater. 141 (2024) 110607.
[13] C. Chen, et al., High-performance mid-infrared fingerprint detection and solution sensing based on quasi-bound states in the continuum, Opt. Commun. 596 (2025) 132499.
[14] C. Hu, et al., High-Q electromagnetically induced transparency and slow-light manipulation via utilizing the quasi-BICs, Opt. Commun. 596 (2025) 132545.
[15] G.K. Yadav, S.K. Metya, Multi Fano resonance-based plasmonic MIM nanosensor for label-free virus detection, IETE J. Res. 70 (9) (2024) 7597–7606.
[16] A. Khodaie, et al., Design of a plasmonic optical biosensor based on a metal-insulator-metal ring resonator for the detection of various bacterial pathogens, Sci. Rep. 15 (1) (2025) 20699.
[17] V.E. Babicheva, Optical processes behind plasmonic applications, Nanomaterials 13 (7) (2023) 1270.
[18] S. Sharma, et al., Sustainable applications of biowaste-derived carbon dots in eco-friendly technological advancements: a review, Mater. Sci. Eng. B 305 (2024) 117414.
[19] Y. Deng, G. Cao, H. Yang, Tunable Fano resonance and high-sensitivity sensor with high figure of merit in plasmonic coupled cavities, Photonics Nanostruct. Fundam. Appl. 28 (2018) 45–51.
[20] X. Yi, J. Tian, R. Yang, Tunable Fano resonance in MDM stub waveguide coupled with a U-shaped cavity, Eur. Phys. J. D 72 (4) (2018) 60.
[21] Y.-F.C. Chau, et al., Enhanced coupling and high-sensitivity multichannel Plasmonic sensor using Split semicircular ring resonators for refractive index and temperature detection, Plasmonics 20 (8) (2025) 5819–5834.
[22] Y.-F. Chou Chau, Enhancing imaging capabilities with a high-sensitivity multichannel optical filter, Micro Nanostruct. 186 (2024) 207732.
[23] Y.-F. Chou Chau, Enhanced plasmonic waveguide sensing performance with a semicircular-ring resonator, Micro Nanostruct. 174 (2023) 207469.
[24] Y.-F. Chou Chau, Multiple-mode bowtie cavities for refractive index and glucose sensors working in visible and near-infrared wavelength ranges, Plasmonics 16 (5) (2021) 1633–1644.
[25] Chou Chao, C.-T. And Y.-F. Chou Chau. Highly sensitive multichannel Fano resonance-based plasmonic sensor for refractive index and temperature sensing application. In Photonics. 2023.
[26] F. Chen, W.X. Yang, Pressure sensor based on multiple Fano resonance in metal–insulator–metal waveguide coupled resonator structure, J. Opt. Soc. Am. B 39 (7) (2022) 1716–1722.
[27] P. Ji, et al., High sensitivity plasmonic refractive index and temperature sensor based on square ring shape resonator with nanorods defects, Opt. Quant. Electron. 54 (3) (2022) 184.
[28] L. Li, F. Chen, Tunable four-band metamaterial absorber and sensor based on a stacking double-ring Dirac semimetal structure design, Phys. Lett. A 544 (2025) 130489.
[29] Z. Li, F. Chen, W. Yang, Magnetic field sensor based on multiple Fano resonance in metal-insulator-metal waveguide coupled with cross-shape resonator, Phys. Scr. 99 (12) (2024) 125527.
[30] X. Tang, et al., Gas concentration and refractive index sensor based on plasmonic induced absorption in metal-insulator-metal waveguide coupled with arc resonators structure, Phys. Scr. 99 (6) (2024) 065561.
[31] L. Arya, et al., Investigation of machine learning algorithms and plasmonic waveguide-based fano resonance sensor for diagnosis of estrogen, Plasmonics 20 (7) (2025) 4931–4941.
[32] M.A. Butt, N.L. Kazanskiy, S.N. Khonina, Highly sensitive refractive index sensor based on plasmonic bow tie configuration, Photon. Sensors 10 (3) (2020) 223–232.

[33] S.-Y. Tseng, et al., Food quality monitor: paper-based plasmonic sensors prepared through reversal nanoimprinting for rapid detection of biogenic amine odorants, ACS Appl. Mater. Interfaces 9 (20) (2017) 17306–17316.
[34] M.N. Hamza, et al., Development of a high-sensitivity triple-band nano-biosensor utilizing Petahertz metamaterials for optimal absorption in early-stage leukemia detection, IEEE Sensors J. 25 (8) (2025) 13955–13973.
[35] J. Wekalao, Design and optimization of a graphene-enhanced plasmonic sensor with machine learning integration for organic compound detection in wastewater, Plasmonics 20 (11) (2025) 1–15.
[36] C.-T.C. Chao, et al., Plasmonic refractive index sensor based on the combination of rectangular and circular resonators including baffles, Chin. J. Phys. 71 (2021) 286–299.
[37] Y.M. Shokorlou, H. Heidarzadeh, H. Bahador, Simulation and analysis of ring shape metal–insulator-metal Plasmonic biosensors for the detection of prostate-specific antigen (PSA), Plasmonics 17 (5) (2022) 2197–2204.
[38] D. Damborska, et al., Nanomaterial-based biosensors for detection of prostate specific antigen, Microchim. Acta 184 (9) (2017) 3049–3067.
[39] P. Jolly, et al., Label-free impedimetric aptasensor with antifouling surface chemistry: a prostate specific antigen case study, Sens. Actuators B 209 (2015) 306–312.
[40] B. Singh, et al., Nanomaterials-based biosensors for the detection of prostate cancer biomarkers: recent trends and future perspective, Adv. Mater. Technol. 8 (13) (2023) 2201860.
[41] V. Liustrovaite, et al., Electrochemical immunosensor for the determination of antibodies against prostate-specific antigen based on ZnO nanostructures, Int. J. Mol. Sci. 24 (6) (2023) 5803.
[42] K. Uchida, et al., A reactive poly (ethylene glycol) layer to achieve specific surface plasmon resonance sensing with a high S/N ratio: the substantial role of a short underbrushed PEG layer in minimizing nonspecific adsorption, Anal. Chem. 77 (4) (2005) 1075–1080.
[43] L. Pasquardini, et al., Optimization of the immunorecognition layer towards Brucella sp. on gold surface for SPR platform, Colloids Surf. B: Biointerfaces 231 (2023) 113577.
[44] M. Butt, N. Kazanskiy, S. Khonina, Metal-insulator-metal waveguide plasmonic sensor system for refractive index sensing applications, Adv. Photonics Res. 4 (7) (2023) 2300079.
[45] S. Khani, M. Danaie, P. Rezaei, Realization of single-mode plasmonic bandpass filters using improved nanodisk resonators, Opt. Commun. 420 (2018) 147–156.
[46] S. Khani, M. Danaie, P. Rezaei, Design of a Single-Mode Plasmonic Bandpass Filter Using a hexagonal resonator coupled to graded-stub waveguides, Plasmonics 14 (1) (2019) 53–62.
[47] E. Beiranvand, M. Danaie, M. Afsahi, An efficient coupling scheme between photonic crystal waveguides and Plasmonic metal-insulator-metal waveguides, Plasmonics 20 (2) (2025) 701–708.
[48] Z.A. Mohamed, Highly sensitive Fano resonance due to coupling between metal-insulator-metal waveguide and semi-ring resonators, Optik 339 (2025) 172530.
[49] Y. Majd Shokorlou, H. Heidarzadeh, Multispectral plasmonic biosensors based on a Penta-supercell metamaterial for detection of prostate-specific antigen: ultrasensitive in LC resonance mode, Biosens. Bioelectron. 217 (2022) 114722.
[50] W.L. Barnes, A. Dereux, T.W. Ebbesen, Surface plasmon subwavelength optics, Nature 424 (6950) (2003) 824–830.
[51] S.A. Maier, Plasmonics: Fundamentals and Applications Vol. 1, Springer, 2007.
[52] S. Babar, J.H. Weaver, Optical constants of cu, ag, and au revisited, Appl. Opt. 54 (3) (2015) 477–481.
[53] S.I. Bozhevolnyi, et al., Channel plasmon subwavelength waveguide components including interferometers and ring resonators, Nature 440 (7083) (2006) 508–511.
[54] N. Liu, et al., Three-dimensional photonic metamaterials at optical frequencies, Nat. Mater. 7 (1) (2008) 31–37.
[55] S.W. Lee, et al., Highly sensitive biosensing using arrays of plasmonic au nanodisks realized by nanoimprint lithography, ACS Nano 5 (2) (2011) 897–904.
[56] M.A. Butt, Metal-insulator-metal waveguide-based plasmonic sensors: fantasy or truth—a critical review, Appl. Theatr. Res. 2 (4) (2023) e202200099.
[57] R. Geiss, et al., Fabrication of free-standing lithium niobate nanowaveguides down to 50 nm in width, Nanotechnology 27 (6) (2016) 065301.
[58] K. Yamada, Silicon Photonic Wire Waveguides: Fundamentals and Applications. Silicon Photonics II: Components and Integration, 2010, pp. 1–29.
[59] S. Sederberg, A. Elezzabi, Coherent visible-light-generation enhancement in silicon-based nanoplasmonic waveguides via third-harmonic conversion, Phys. Rev. Lett. 114 (22) (2015) 227401.
[60] Y.-F.C. Chau, et al., Strong and tunable plasmonic field coupling and enhancement generating from the protruded metal nanorods and dielectric cores, Results Phys. 13 (2019) 102290.
[61] N.R. Sabaruddin, et al., Designing a broadband terahertz metamaterial absorber through bi-layer hybridization of metal and graphene, Plasmonics 19 (6) (2024) 3259–3272.
[62] I.M. Mackay, K.E. Arden, A. Nitsche, Real-time PCR in virology, Nucleic Acids Res. 30 (6) (2002) 1292–1305.
[63] D. Wild, The Immunoassay Handbook: Theory and Applications of Ligand Binding, ELISA and Related Techniques, Newnes, 2013.
[64] J. Homola, Surface Plasmon resonance sensors for detection of chemical and biological species, Chem. Rev. 108 (2) (2008) 462–493.
[65] M.C. Estevez, M. Alvarez, L.M. Lechuga, Integrated optical devices for lab-on-a-chip biosensing applications, Laser Photonics Rev. 6 (4) (2012) 463–487.
[66] J.N. Anker, et al., Biosensing with plasmonic nanosensors, Nat. Mater. 7 (6) (2008) 442–453.
[67] K.M. Mayer, J.H. Hafner, Localized surface plasmon resonance sensors, Chem. Rev. 111 (6) (2011) 3828–3857.
[68] S. Guchhait, et al., A metal-insulator-metal waveguide-based plasmonic refractive index sensor for the detection of nanoplastics in water, Sci. Rep. 14 (1) (2024) 21495.
[69] M. Danaie, L. Hajshahvaladi, E. Ghaderpanah, A single-mode tunable plasmonic sensor based on an 8-shaped resonator for cancer cell detection, Sci. Rep. 13 (1) (2023) 13976.
[70] M.S. Moghtader, H. Heidarzadeh, A. Khodaie, Supercell-enhanced multimodal plasmonic sensor for high-fidelity antigen detection via refractive index modulation, Sci. Rep. 15 (1) (2025) 22322.
[71] R. Rahad, N. Hossain, A. Hossain, Enhanced alcohol detection using surface plasmon polariton dependent MIM plasmonic sensor, Plasmonics 20 (3) (2025) 1331–1340.
[72] M.A. Butt, Numerical assessment of a metal-insulator-metal waveguide-based plasmonic sensor system for the recognition of tuberculosis in blood plasma, Micromachines 14 (4) (2023) 729.
[73] P. Rishi, et al., Next-generation phi-configured graphene-enhanced MIM Nanobiosensor for high-sensitivity Cancer diagnostics, Plasmonics 20 (8) (2025) 6795–6805.
[74] S. Khani, P. Rezaei, M. Rahmanimanesh, Machine learning analysis of a Fano resonance based plasmonic refractive index sensor using U shaped resonators, Sci. Rep. 15 (1) (2025) 23857.
[75] S. Khani, M. Hayati, Optical biosensors using plasmonic and photonic crystal band-gap structures for the detection of basal cell cancer, Sci. Rep. 12 (1) (2022) 5246.
[76] S. Khani, M. Hayati, An ultra-high sensitive plasmonic refractive index sensor using an elliptical resonator and MIM waveguide, Superlattice. Microst. 156 (2021) 106970.
[77] Z. Ayareh, et al., Accessible sensing sites in metal–insulator–metal Plasmonic nanostructure for biosensing applications, ACS Appl. Mater. Interfaces 17 (38) (2025) 53122–53130.
[78] C.-Y. Chang, et al., Flexible localized surface Plasmon resonance sensor with metal–insulator–metal Nanodisks on PDMS substrate, Sci. Rep. 8 (1) (2018) 11812.
[79] L.P. Hackett, et al., Spectrometer-free Plasmonic biosensing with metal-insulator-metal Nanocup arrays, ACS Sens. 3 (2) (2018) 290–298.